

AperTO - Archivio Istituzionale Open Access dell'Università di Torino

Nature and Topology of Metal-Oxygen Binding Sites in Zeolite Materials: 170 High-Resolution EPR Spectroscopy of Metal-Loaded ZSM-5

This is the author's manuscript

Original Citation:

Availability:

This version is available <http://hdl.handle.net/2318/1711965> since 2019-09-18T13:07:32Z

Published version:

DOI:10.1002/anie.201906488

Terms of use:

Open Access

Anyone can freely access the full text of works made available as "Open Access". Works made available under a Creative Commons license can be used according to the terms and conditions of said license. Use of all other works requires consent of the right holder (author or publisher) if not exempted from copyright protection by the applicable law.

(Article begins on next page)

Nature and topology of metal-oxygen binding sites in zeolite materials: ^{17}O High-resolution EPR spectroscopy of metal loaded ZSM-5.

E. Morra, §^[a] M. Signorile, §^[a] E. Salvadori, ^[a] S. Bordiga, ^[a] E. Giamello, ^[a] M. Chiesa *^[a]

We dedicate this work to the memory of our common friend and colleague Carlo Lamberti (1964–2019)

Abstract: Determining structural models is pivotal to any rational understanding and development of heterogeneous catalytic systems. A paradigmatic case is represented by open-shell metals supported on oxides, where the catalytic properties crucially depend on the nature of metal-oxygen bonds and the extent of charge and spin transfer. Through a combination of selective ^{17}O isotopic enrichment and the unique properties of open-shell s-state monovalent group 12 cations, we derive a site-specific topological description of active sites in a MFI zeolite. We show that just a few selected sites out of all possible are populated, that the relative occupancies depend on the specific properties of the metal and we provide maps of charge and spin transfer at the metal-oxygen interface. This approach is not restricted to zeolite materials, rather it is applicable to any catalysts supported on oxygen containing materials.

The nature of the metal-oxide bonding interaction is one of the primary factors affecting the catalytic activity of heterogeneous catalysts based on metals stabilized on inorganic supports.¹ Tiny metal nanoparticles 2-10 nm in size,² small clusters³ and even single atoms⁴, stabilized on oxide surfaces or in the cages and channels of zeolite materials⁵ exhibit surprising catalytic properties⁶, intimately connected with the nature of the chemical interactions between the metal and the oxide support. The whole range of chemical bonding interactions are displayed at the metal/oxide interface, from weak dispersion forces to covalent bonds arising from the mixing of metal and oxide orbitals. Understanding and tuning these interactions is key to tailor new catalysts, a notoriously difficult task in view of the complexity of oxide surfaces.

A critical step in the emergence of rational catalyst design is therefore the structural determination of surface species with molecular-level precision. This characterization challenge requires a combination of spectroscopic methods (e.g., UV-Vis, IR, EXAFS, etc.), possibly complemented by computational approaches.⁷ Among various spectroscopic techniques, solid-state NMR⁸ and EPR⁹ methods are unique tools for the determination of the structure of oxide materials at the atomistic level. In the case of porous alumino-silicate oxides (zeolites)²⁹Si and ²⁷Al solid-state NMR experiments have been crucial for the determination of the number of crystallographic sites, their

connectivity and their local coordination environments and structure. By contrast, ^{17}O NMR in spite of the obvious potential of this isotope as a probe of local structure, disorder and dynamics, is far less common, due to the low natural abundance (0.037%), high nuclear spin ($I=5/2$) and low magnetic moment.¹⁰⁻¹²

Even less frequent are EPR studies involving the incorporation of ^{17}O at the surface of inorganic oxides¹³⁻¹⁸. EPR is a spectroscopic technique that allows detection of paramagnetic centers and their coupled magnetic nuclei with spatial resolution from the atomic up to the nanometer scale.¹⁹ The technique can selectively probe metal ions with open-shell electronic configurations, which are often directly involved in catalytic cycles acting - from the EPR perspective - as probes directly reporting on their own activity. As in the case of NMR, ²⁷Al, ²⁹Si and ¹H, two-dimensional EPR (HYSCORE) and ENDOR spectroscopies have been used to obtain exquisite details on the local coordination of catalytically relevant metal ions in zeolite materials²⁰⁻²³, but no information relative to the metal-oxygen bond and electron delocalization over the zeolite framework are directly available. This very information can be gathered through the detection of hyperfine interactions (*hfi*) of ^{17}O labelled lattice sites.

Zn⁺ and Cd⁺ metal ions, characterized by a *ns*¹ electron configuration have recently emerged as promising catalytic active species in the context of small molecules activation.²⁴⁻²⁸ Taking advantage of the simplicity of their electronic configuration, in this contribution, these chemical species are used as paramagnetic probes to unravel the nature of the chemical bond and the topology of metal binding sites in zeolites by monitoring the extent of the delocalization of their unpaired electron onto a ^{17}O enriched ZSM-5 zeolite framework. Moreover, periodic and cluster quantum chemical calculations provide insight into the site-dependent energetics of the metal-zeolite interaction. Taking the industrially relevant ZSM-5 zeolite as an example, this paper shows how this combined approach enables the identification and characterization of distinctly different active sites in a macro- and microscopically heterogeneous zeolite catalyst, revealing unique details on the metal to oxygen orbital mixing and on the structure and topology of metal ions in complex oxide systems.

The Continuous Wave (CW)-EPR spectra of Zn²⁹ and Cd³⁰ in ZSM-5 are indicative of Zn⁺ and Cd⁺ species and are characterized by narrow lines and a *g* anisotropy increasing from Zn to Cd, which reflects the increasing spin orbit coupling (Figure 1a and 1c). Hyperfine interaction with framework ²⁷Al, ²⁹Si and ¹H nuclei, detected through advanced pulsed experiments, provide clear-cut evidence for the localization of mononuclear metal cations at the acidic Brønsted sites of H-ZSM-5, in close proximity of an Al ion.^{29,30}

Evaporating the two metals over the ^{17}O exchanged zeolites leads to new CW-EPR spectra characterized by a complex hyperfine pattern reflecting the degree of spin delocalization onto the

[a] Dr. E. Morra, Dr. M. Signorile, Dr. E. Salvadori, Prof. S. Bordiga, Prof. E. Giamello, Prof. M. Chiesa
Department of Chemistry
University of Torino
Via Giuria, 9 10125 – Torino, Italy.
E-mail: mario.chiesa@unito.it

§ These two Authors contributed equally

Supporting information for this article is given via a link at the end of the document.

framework oxygen anions and the contribution of different ^{17}O isotopomers. In the case of Zn, simulation of the spectra (Supporting information, section S4.1) shows that the spectral pattern is the superposition of at least three main sub-spectra characterized by zero, six and eleven hyperfine lines, reflecting the number of isotopically labelled coordinated oxygens (0, 1 and 2 respectively).

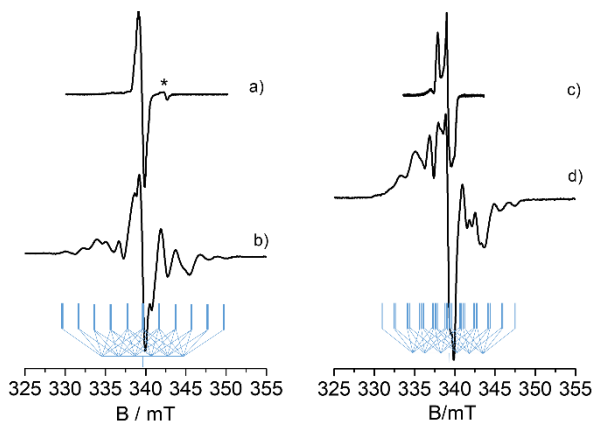


Figure 1. a) X-band CW EPR spectra of a) Zn^+ species in ZSM-5; b) Zn^+ species in ^{17}O exchanged ZSM-5; c) Cd^+ species in ZSM-5 and d) Cd^+ species in ^{17}O exchanged ZSM-5. All spectra were recorded at room temperature. The blue stick diagrams indicate the ^{17}O hyperfine patterns characteristic of two equivalent (b) or nearly equivalent (d) $I=5/2$ nuclei..

From the relative abundances of these three isotopomers, deduced by the simulation analysis, we estimate a local enrichment level of approximately 70% (Supporting Information, Figure S5). Such a high level of enrichment under the adopted mild conditions, reflects the high reactivity of the Al-O-Si bridging oxygens, in line with ^{18}O exchange experiments.³¹ Importantly, the presence of an 11-line pattern demonstrates that two equivalent oxygen nuclei are interacting with the unpaired electron of Zn^+ , pointing to a situation where the metal cation is bound to two oxygen anions with a pseudo- C_{2v} local symmetry. For Cd^+ , CW-EPR suggests a lower coordination symmetry with at least two non-equivalent oxygens, as exemplified by the stick diagrams in Figure 1. Q-band HYSCORE experiments were performed to fully identify all the components of the ^{17}O hyperfine couplings, including small couplings, which may not be observed in the CW spectra. HYSCORE³² is a bidimensional technique, where the coordinates of the measured off-diagonal cross-peaks can be used to recover the identity of the nuclei coupled to the electron spin (Larmor frequencies) and the magnitude of their hyperfine interactions. The HYSCORE spectra of Zn^+ and Cd^+ in ZSM-5 zeolite (Figure 2) show ^{17}O correlation peaks in both (-,+) and (++) quadrants as well as ^{27}Al correlation peaks in the (+,+) quadrant. These latter were discussed elsewhere.^{29,30} Two set of oxygen cross-peaks, are found in the (+,+) quadrant Figures 2b and 2d), centered at the ^{17}O nuclear Larmor frequency

($\nu_0 \approx 7.5$ MHz), and separated approximately by the hfi constant A . The full set of hfi values (Table 1) was estimated through the simulation of the HYSCORE spectra taken at different observer positions (Supporting Information, Figures S8 and S9). For both Zn^+ (Figure 2b) and Cd^+ (Figure 2d), isotropic hfi constants of the order 8 MHz and 2 MHz were observed.

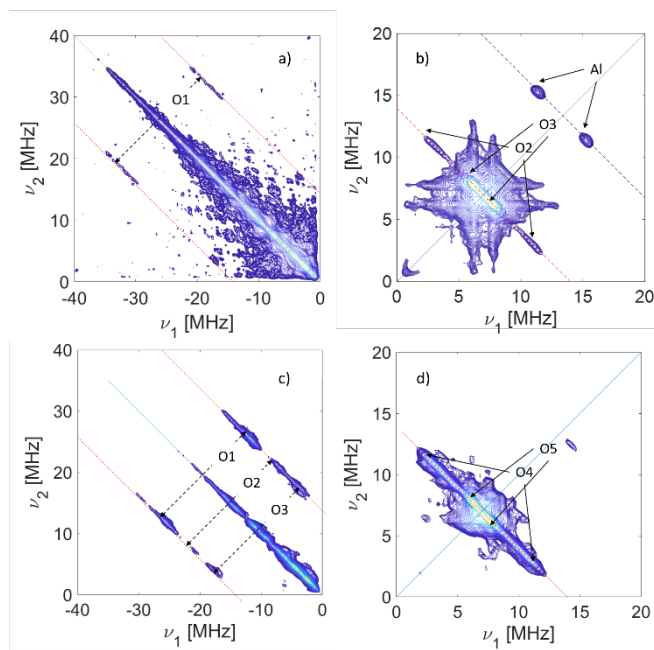


Figure 2. Representative ^{17}O Q-band HYSCORE spectra of Zn^+ (a) and b)) and Cd^+ (c) and d)) obtained at echo maximum intensity. Due to the poor signal to noise ratio the spectra of Zn^+ have been symmetrized. Spectra recorded at other observer positions and unsymmetrized Zn^+ spectra are reported in the supporting information. The (-,+) and the (+,+) quadrants are plotted independently in order to optimize the resolution and contour level of the different signals. ^{17}O cross-peaks are indicated by arrows. Signals due to ^{27}Al are also indicated. Spectra acquired with different τ values (100 ns, 144 ns and 214 ns) were added together after Fourier transformation to avoid blind spot effects. All spectra were recorded at 70 K.

The other sets of off-diagonal cross peaks are found in the (-,+) quadrant centered at $A/2$ and separated by approximately $2\nu_0$, as expected in the strong-coupling limit.³³ Due to the large isotropic hfi the nuclear quadrupole interaction (computed to be of the order of $e^2qQ/h = 4.5$ MHz, Table S1, Supporting Informations) does not have a significant influence on the spectrum (Supporting Information section S4.2). For the Zn^+ case (Figure 2a) a single pair of elongated cross peaks labelled O1 in Figure 2a are observed, corresponding to an hfi of ≈ 60 MHz. A richer (-,+) quadrant is observed for Cd^+ , with at least three sets of off-diagonal cross peaks labelled (O1-O3) in Figure 2c, with hfi ranging from ≈ 50 MHz to 25 MHz and proving the presence of at least three directly coordinated oxygens. The complete set of ^{17}O hfi couplings obtained by simulation of the HYSCORE experiments are listed in Table 1.

Table 1. Experimental spin-Hamiltonian parameters derived from the simulation of the EPR and HYSCORE spectra. Due to relatively large isotropic contributions in both g and A tensors, the relative orientations of the hf tensors was immaterial. In the simulations the values obtained by DFT computations (see Figure S7) were used. ^a values from Ref.29, ^b value from Ref.30. The A tensor components are given in units of MHz, ^c ± 20 , ^d ± 2

Metal	g tensor ^a			⁶⁵ Zn A tensor ^c				¹⁷ O A tensor ^d				²⁷ Al A tensor ^a				
	g_1	g_2	g_3	a_{iso}	T_1	T_2	T_3	Site	a_{iso}	T_1	T_2	T_3	a_{iso}	T_1	T_2	T_3
Zn	1.9951	1.9984	2.0015	1525	-5	-5	10	O(1)	-52	+5	+5	-10	3.4	-0.6	-0.7	1.3
								O(2)	-8	+0.9	+0.9	-1.8				
								O(3)	-2	+0.5	+0.5	-1				
Cd	1.9891	1.9932	2.0007	-10683	63	44	-107	O(1)	-40	+5	+5	-10	1.8	-0.6	-0.7	1.3
								O(2)	-29	+5	+5	-10				
	1.9875	1.9918	2.0007					O(3)	-21	+2	+2	-4				
								O(4)	-8	+0.9	+0.9	-1.8				
								O(5)	-2	+0.5	+0.5	-1				

Table 2. Spin-Hamiltonian parameters calculated through DFT calculations on atomistic models. The A tensor components are given in MHz; the d(Zn-O) and d(Cd-O) distances are given in Å. The g tensor elements and the hfi tensors are calculated using the ORCA code. Spin on metals obtained from Mulliken population analysis (Mulliken spin population on relevant oxygen atoms is provided in Table S7 of Supporting Information). Additional computed parameters (relative tensors orientations, quadrupole tensors) are provided in Table S1 of Supporting Information.

Site	g tensor			Spin	⁶⁵ Zn A tensor				¹⁷ O A tensor				d(Zn-O)	²⁷ Al A tensor			
	g_1	g_2	g_3		a_{iso}	T_1	T_2	T_3	a_{iso}	T_1	T_2	T_3		a_{iso}	T_1	T_2	T_3
T7	1.9920	1.9963	2.0023	0.84	1331	-9.7	-6.3	16.0	-60.8	7.8	8.1	-15.8	2.086	5.3	-0.2	-0.5	0.7
									-60.2	8.2	8.4	-16.6	2.099				
T8	1.9946	1.9975	2.0023	0.81	1466	-7.8	-5.7	13.5	-55.8	9.3	9.5	-18.8	2.133	0.5	-0.2	-0.5	0.7
									-28.4	6.2	6.3	-12.5	2.231				
									-16.4	-6.3	3.1	3.2	2.781				
									-9.9	1.6	-3.3	1.7	3.182				
T10	1.9921	1.9965	2.0023	0.83	1341	-9.5	-6.2	15.7	-56.7	7.9	8.3	-16.1	2.092	4.6	-0.2	-0.5	0.7
									-56.1	8.4	8.6	-17.0	2.114				
T7	1.9801	1.9880	2.0022	0.86	-7548	47.4	34.4	-81.8	-45.2	6.7	7.0	-13.7	2.320	3.6	-0.2	-0.4	0.6
									-44.7	7.1	7.2	-14.3	2.340				
T8	1.9861	1.9903	2.0022	0.82	-8188	37.7	29.3	-67.0	-44.7	8.2	8.3	-16.4	2.384	-0.4	0.0	-0.5	0.5
									-27.8	-8.8	4.3	4.5	2.656				
									-15.7	2.3	-4.7	2.4	3.001				
									-9.1	3.0	3.1	-6.1	2.669				
T10	1.9889	1.9924	2.0023	0.81	-8648	30.4	24.2	-54.6	-37.0	5.7	5.8	-11.5	2.405	-0.6	-0.3	-0.4	0.7
									-30.4	6.7	6.6	-13.3	2.603				
									-12.9	-4.6	2.3	2.2	3.114				
									-10.5	2.5	-4.8	2.4	3.089				

The EPR data alone, thus indicate a distinctive and well defined coordination for Zn⁺ and Cd⁺ adsorbed ions. Considering only the strongly coupled oxygens, single Zn⁺ ions are bound at surface oxygen sites where they strongly interact with two equivalent (or nearly equivalent) oxygens, while Cd⁺ ions display an interaction with at least three oxygen ions with different couplings. The hosting site of Zn⁺ can be treated as a bidentate macroligand giving rise to effective diagonal coordination with approximate C_{2v} local symmetry, whereas a distorted tripodal structural arrangement can be inferred for Cd⁺, with one stronger and two weaker bonds. In both cases electron spin density is found to be delocalized over more distant framework oxygens, as indicated by similar couplings in the range 2-8 MHz, observed in the (+,+) quadrant of the HYSCORE spectra.

The isotropic (¹⁷⁰ a_{iso}) and dipolar (¹⁷⁰ T) components of the hfi extracted from the simulation analysis (Table 1) may be compared with the corresponding atomic values for assessment of the spin

density repartition on the O 2s and 2p orbitals (see Supporting Information, section S5). In the Zn⁺ case, the electron spin population in the s- and p-type oxygen orbitals can be estimated to be $\rho_s \approx 1\%$ and $\rho_p \approx 2\%$, corresponding to a spin density delocalization $\rho_O = 6\%$ over the two binding oxygens. A similar degree of delocalization is found also in the case of Cd⁺, although distributed over at least three main binding oxygen ions. These values are in good agreement with the Mulliken spin population analysis (Supporting Information, Table S7). Exploiting the presence of sufficiently abundant magnetically active isotopes - ⁶⁵Zn (ab. 4.11%), ¹¹¹Cd and ¹¹³Cd (ab. 12.75% and 12.26% respectively) an experimentally derived spin density on the Zn and Cd atoms of the order of $\rho_{Zn(total)} = 77\%$ and $\rho_{Cd(total)} = 84\%$ ²⁴ is estimated, in reasonable agreement with the computed values (81-86%, Table 2) and the spin delocalization over the binding oxygens. It thus emerges that the metal oxygen bond displays a non-negligible covalent character with an approximately 10%

participation of the oxygens valence orbitals to the SOMO. Comparison may be set at this stage with K atoms (isoelectronic with Zn^{2+}) in an analogous coordination at the surface of $Mg^{17}O$ where $\rho_K = 51\%$ and $\rho_O = 0.8\%$ were reported.¹³ To note that whereas the sum of ρ_O and ρ_{metal} for Zn/Cd is close to 100% (i.e. the total spin density), this is not the case for K. Indeed this reflects the different nature of the chemical bond: a strong polarization interaction for K on MgO¹³ and an ionic-covalent bond character for Zn^{2+} and Cd^{2+} in the channels of ZSM-5.

To translate the spectroscopic results into an atomistic model, DFT calculations were performed for three representative sites of the MFI framework. These sites, namely T7, T8 and T10, were chosen because they show slightly different local environments and have been consistently indicated - beside some minor discrepancies in the relative ranking - as preferential Al substitution sites by diffraction studies on Ti/Cs substituted ZSM-5.³⁴⁻³⁶ Site T7 sits at the zeolite channels intersection, T8 belongs to a straight channel along the *b* axis and T10 is placed in the sinusoidal channels parallel to the *a* axis (Supporting information, Figure S2). The Spin-Hamiltonian parameters obtained through DFT calculations on these models are reported in Table 2

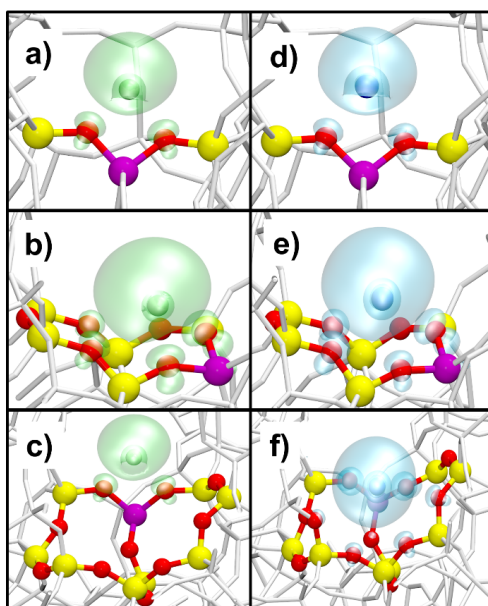
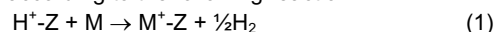


Figure 3. Spin density plots for Zn^{2+} (a) to (c) and Cd^{2+} (d) to (f) for the three different T sites T7 (a) and (d), T8 (b) and (e)) and T10 (c) and (f)). Some relevant atoms in the local environment of the paramagnetic centers are represented by ball-and-stick (color code: green Zn, blue Cd, purple Al, red O, yellow Si). The remaining framework atoms are represented by grey sticks.

The metal-oxygen coordination for Zn^{2+} and Cd^{2+} ions at the different sites (T7, T8 and T10) show some interesting characteristics. In particular, no significant differences in terms of geometry are observed in the case of Zn^{2+} at sites T7 and T10, showing a local C_{2v} symmetry with metal-oxygen distances in the order of 2.1 Å. A very similar coordination is observed for Cd^{2+} coordinated at site T7, presenting the same local environment as in the case of Zn^{2+} , with just slightly elongated metal-oxygen distances (~2.3 Å), consistent with the increased ionic radius. Higher coordinated environments are instead observed for both Zn^{2+} and Cd^{2+} at site T8 and for Cd^{2+} also at site T10. In detail, both

ions assume a distorted square planar coordination at T8, where all oxygens are found in the 2.1-3.2 Å distances range from the Zn^{2+} ion (2.4-3.0 Å in the case of Cd^{2+}). Cd^{2+} at the T10 site shows the richest coordination environment, with the two closest oxygens at approximately 2.4 Å and 2.6 Å and other three falling in the 3.0-3.3 Å distances range. The topological analysis of the electron density distribution and the evaluation of the critical points (Supporting Information, section S6)³⁷ follows the spin density distribution trends shown in Figure 3. The critical points are locations where the gradient of the electron density is zero and allow the identification of bond paths. Two such points can be identified between the Zn cation and the framework oxygens of the Si-O-Al moieties for sites T7, and T10, while four critical points are found for site T8. In the case of Cd^{2+} a similar situation is observed for T7 and T8, while different bond paths, characterized by 5 critical points with both Al-O-Si and Si-O-Si bridging oxygens are obtained for site T10. These results are in agreement with the richness of the ^{17}O HYSCORE spectra of Cd indicating a non-negligible reactivity of the Si-O-Si bridging oxygens, even under the mild reaction conditions adopted in this work.

These geometrical features are reflected in the computed **g** and **A** tensors, which show nearly identical values for Zn^{2+} at sites T7 and T10 all in good agreement with the experiments. Different values are computed for T8. While this site reproduces ^{17}O couplings of the order of 10 MHz, in line with the experimentally observed 8 MHz, significant departure from magnetic equivalence of the oxygens and a negligible coupling to ^{27}Al are at odds with both CW and pulse experiments. Although the role of T8 in stabilizing Zn^{2+} ions, cannot be excluded, it appears to be minor, leaving T7 and T10 as the most likely sites. This is also in agreement with the Boltzmann relative population of the three sites, estimated according to the following reaction:



where Z represents the zeolite framework. Although for all sites a negative ΔE is found, T8 shows the least negative value upon Zn^{2+} substitution, resulting in a mere population contribution of the order of 1%, whereas T7 and T10 are predicted to be populated in a 1:2 ratio (see Supporting Information).

In the case of Cd the different adsorption geometry for sites T7 and T10 leads to spin Hamiltonian parameters displaying significant differences. At variance with the case of Zn^{2+} , the calculated ^{17}O hyperfine coupling constants indicate for site T10 a clear asymmetry in the ^{17}O *hfi* of the two strongly coupled oxygens and significant spin density on other framework oxygens. These are in qualitative agreement with the experimental results, including the 8 MHz coupling observed in the HYSCORE spectra. Significant differences are also computed for the ^{27}Al *hfi* couplings for the two sites, with a_{iso} =3.6 MHz for T7 and closely zero for T10 to be compared with the sole experimentally determined value of 1.8 MHz. The computed spin Hamiltonian parameters for site T8 are in this case similar to those of T10, while based on the energy evaluation related to Eq. 1, the highest population is predicted for site T10, with $T10 > T8 > T7$.

To summarize, by combining the experimental and theoretical results, a model for the binding sites of group 12 monovalent cations Zn^{2+} and Cd^{2+} emerges. ^{17}O high resolution EPR methods provide an unprecedented level of details in the description of the ensemble of atoms that constitute the metal binding site allowing the determination of the full spin density distribution, pointing to a non negligible degree of covalency with approximately 10% delocalization of the metal electron spin over the oxide ions.

These features are correctly reproduced by theoretical calculations, where the cations are stabilized at specific morphological sites of the zeolite. Interestingly, while the T7 and T8 sites lead to very similar properties for both Zn⁺ and Cd⁺, site T10 is instead clearly discriminated by the softer Cd⁺ ion.

We consider the results presented here to be a general methodology based on specific ¹⁷O isotopic labelling, theoretical modelling and the unique selectivity of EPR spectroscopy towards catalytically active paramagnetic species. The scope of the approach is not limited to *ns*¹ states but can be extended to industrially relevant *d* transition metal ions such as V⁴⁺ or Cu²⁺. Experiments are currently being performed in our laboratory towards this direction. We expect this approach to be useful in developing an atomistic understanding of metal-oxide based catalysts, in which highly synergistic interactions between metals and oxide supports are the basis of unique chemical reactivity and catalytic performances.

Experimental Section

The isotopic enrichment of the zeolite framework was carried out by successive hydration and dehydration cycles of the sample, exposing the solid to vapors of H₂¹⁷O (86% isotopic enrichment supplied by Icon Services New Jersey). Since the framework substitution of ¹⁶O by ¹⁷O relies on a mild steaming (120 °C for 2 h, in presence of H₂¹⁷O vapors), IR spectroscopy of adsorbed pyridine was used to verify that no dealumination of the framework occurs under these conditions (Supporting Information). It is to note that ¹⁷O isotopic enrichment can be extremely costly, however, for EPR purposes cost- and atom-efficient protocols such that one described can be used, exploiting the readily exchange of lattice oxide ions with the oxygen of adsorbed H₂O, while keeping highly crystalline frameworks.³¹ Experimental and computational details are provided in the Supporting Information (Section S2).

Acknowledgements

The simulations were performed on resources provided by UNINETT Sigma2 - the National Infrastructure for High Performance Computing and Data Storage in Norway, under project number NN9381K

Keywords: Heterogeneous Catalysis • Zeolites • EPR • HYSCORE • isotopic labelling

References

- ¹ G. Pacchioni, H.-J. Freund, *Chem. Soc. Rev.*, **2018**, 47, 8474-8502.
- ² Y. Xia, H. Yang, C. T. Campbell, *Acc. Chem. Res.*, **2013**, 46, 1671-1672.
- ³ U. Heiz, E. L. Bullock, *J. Mater. Chem.*, **2004**, 14, 564-577.
- ⁴ B. R. Cuenya, F. Behafarid, *Surf. Sci. Rep.*, **2015**, 70, 135-187.
- ⁵ M. J. Climent, A. Corma, S. Iborra, *Chem. Rev.*, **2011**, 111, 1072-1133.
- ⁶ J. Oliver-Meseguer, J. R. Cabrero-Antonino, I. Domínguez, A. Leyva-Pérez, A. Corma, *Science*, **2012**, 338, 1452-1455.
- ⁷ A. Zecchina, S. Bordiga, E. Groppo in *Selective Nanocatalysts and Nanoscience Concepts for Heterogeneous and Homogeneous Catalysis* (Eds.: A. Zecchina, S. Bordiga, E. Groppo) Wiley-VCH, Weinheim, **2011** pp. 1-27.
- ⁸ C. Coperet W.-C. Liao, C. P. Gordon, Ta-C. Ong *J. Am. Chem. Soc.*, **2017**, 139, 10588-10596.
- ⁹ D. Goldfarb, *Phys. Chem. Chem. Phys.*, **2006**, 8, 2325-2343
- ¹⁰ L. M. Bull, B. Bussemer, T. Anupöld, A. Reinhold, A. Samoson, J. Sauer, A. K. Cheetham, R. Dupree, *J. Am. Chem. Soc.*, **2000**, 122, 4948-4958.
- ¹¹ M. Profeta, F. Mauri, C. J. Pickard, *J. Am. Chem. Soc.*, **2003**, 125, 541-548.
- ¹² L. Peng, Y. Liu, N. Kim, J. E. Readman, C. P. Grey, *Nature Mater.*, **2005**, 4, 216-219.
- ¹³ M. Chiesa, E. Giamello, C. Di Valentin, G. Pacchioni, Z. Sojka, S. Van Doorslaer, *J. Am. Chem. Soc.*, **2005**, 127, 16935-16944.
- ¹⁴ N. B. Wong, J. H. Lunsford *J. Chem. Phys.* 1971, 55, 3007-3012.
- ¹⁵ S. Livraghi, S. Maurelli, M. C. Paganini, M. Chiesa, E. Giamello, *Angew. Chem. Int. Ed.* **2011**, 50, 8038-8040.
- ¹⁶ M. Chiesa, E. Giamello, C. Di Valentin, G. Pacchioni, *Chem. Phys. Lett.*, **2005**, 403, 124-128
- ¹⁷ S. Livraghi, M. Chiesa, M. C. Paganini, E. Giamello, *J. Phys. Chem., C*, **2011**, 115, 25413-25421
- ¹⁸ V. Brezová, Z. Barbieriková, M. Zúkalová, D. Dvoranová, L. Kavan, *Catal., Today*, **2014**, 230, 112-118.
- ¹⁹ M. M. Roessler, E. Salvadori, *Chem. Soc. Rev.*, **2018**, 47, 2534-2553.
- ²⁰ P. Carl, D. Vaughan, D. Goldfarb *J. Am. Chem. Soc.*, **2006**, 128, 7160-7161.
- ²¹ P. Pietrzyk, T. Mazur, K. Podolska-Serafin, M. Chiesa, Z. Sojka, *J. Am. Chem. Soc.*, **2013**, 135, 15467-15478.
- ²² M. Chiesa, V. Meynen, S. Van Doorslaer, P. Cool, E. Vansant, *J. Am. Chem. Soc.*, **2006**, 128, 8955-8963.
- ²³ E. Morra, E. Giamello, M. Chiesa *J. Mag. Reson.*, **2017**, 280, 89-102.
- ²⁴ G. Chen, Y. Zhao, L. Shang, G. I. N. Waterhouse, X. Kang, Li-Zhu Wu, C.-Ho Tung, T. Zhang, *Adv. Sci.*, **2016**, 3, 1500424
- ²⁵ A. Oda, H. Torigoe, A. Itadani, T. Ohkubo, T. Yumura, H. Kobayashi, Y. Kuroda *J. Am. Chem. Soc.* **2013**, 135, 18481-18489.
- ²⁶ G. Qi, J. Xu, J. Su, J. Chen, X. Wang, F. Deng, *J. Am. Chem. Soc.*, **2013**, 135, 6762-6765.
- ²⁷ L. Li, G. D. Li, C. Yan, X. Y. Mu, X. L. Pan, X. X. Zou, K. X. Wang, J. S. Chen, *Angew. Chem., Int. Ed.* **2011**, 50, 8299-8303.
- ²⁸ J.-F. Wang, D. Wang, H. Zenga, Z.-F. Zhou, *RSC Adv.*, **2015**, 5, 77490-77494.
- ²⁹ E. Morra, G. Berlier, E. Borfecchia, S. Bordiga, P. Beato, M. Chiesa, *J. Phys. Chem. C*, **2017**, 121, 14238-14245.
- ³⁰ E. Morra, M. Chiesa, *J. Phys. Chem. C*, **2018**, 122, 9515-9522.
- ³¹ R. von BaHmoos, W. M. Meier, *J. Phys. Chem.*, **1982**, 86, 2698-2700.
- ³² P. Höfer, A. Grupp, H. Nebenführ, M. Mehring, *Chem. Phys. Lett.*, **1986**, 132, 279-282.
- ³³ S. Van Doorslaer, *eMagRes*, **2017**, 6, 51-70.
- ³⁴ D.H. Olson, N. Khosrovani, A.W. Peters, B.H.J. Toby, *J. Phys. Chem. B*, **2000**, 104, 4844-4848.
- ³⁵ N. H. Heo, C. W. Kim, H. J. Kwon, G. H. Kim, S. H. Kim, S. B. Hong, K. J. Seff, *J. Phys. Chem. C*, **2009**, 113, 19937-19956.
- ³⁶ C. W. Kim, N. H. Heo, K. Seff, *J. Phys. Chem. C*, **2011**, 115, 24823-24838.
- ³⁷ R. F. W. Bader, *Atoms in Molecules. A Quantum Theory*; Oxford University Press: Oxford, UK, **1990**.

Supporting Information

- S1. Q-band ESE detected EPR of Zn⁺ in ZSM5 – ⁶⁷Zn hyperfine interactions and Euler rotation of hyperfine and quadrupolar tensors to g-tensor**
- S2. Experimental and computational details**
- S3. Determination of acid sites density of the parent and the steamed samples**
- S4. EPR Spectra Simulation**
- S5. Calculation of spin density from the isotropic and the dipolar parts of the ¹⁷O hyperfine couplings.**
- S6. Bader Analysis of the electron density distribution**
- S7. Basis sets adopted in the calculations (CRYSTAL format)**

S1. Q-band ESE detected EPR of Zn⁺ in ZSM5 – ⁶⁷Zn hyperfine interactions

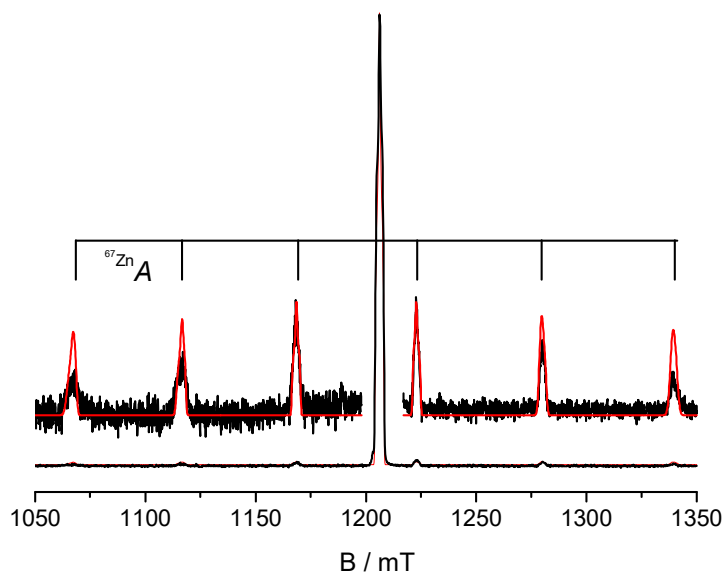


Figure S1 Experimental (black) and simulated (red) Q-band ESE detected EPR spectrum of Zn⁺ ions in ZSM-5. The stick diagram evidences the natural abundance ⁶⁷Zn hyperfine lines. (⁶⁷Zn $I=5/2$ ab 4.11%). The spectrum was recorded at room temperature with the following conditions: $\pi/2=16$ ns, $\tau=200$ ns $\nu=33.824$ GHz. The parameters extracted from the simulation are listed in Table 1 of the main text.

Table S1. Computed Euler rotation of hyperfine and quadrupolar tensors to g-tensor. First rotation by alpha around z; second rotation by beta around y'; third rotation by gamma around z''. A positive sign corresponds to a clockwise rotation, a negative sign to a counterclockwise rotation. The tensor values are in MHz, while angles are in degrees.

Site	g tensor			17O A tensor			17O Euler rotation of A tensor to g-tensor			17O Quadrupole tensor			17O Euler rotation of Q tensor to g-tensor			
	gx	gy	gz	Ax	Ay	Az	Alpha	Beta	Gamma	Qx	Qy	Qz	Alpha	Beta	Gamma	
Zn	T7	1,9920	1,9963	2,0023	-52,0	-51,7	-76,8	174,0	19,5	-174,4	-0,17	0,200	-0,030	-15,4	12,7	7,3
					-53,1	-52,8	-76,7	1,0	19,0	-1,8	-0,185	0,210	-0,025	177,7	15,8	-177,2
	T8	1,9946	1,9975	2,0024	-22,2	-22,1	-40,8	-155,4	27,7	150,0	-0,18	0,180	0,000	-68,0	21,2	97,0
					-46,4	-46,3	-74,6	-15,0	26,2	22,0	-0,17	0,200	-0,030	-111,4	29,5	71,1
					-8,3	-13,2	-8,2	-36,6	38,4	50,6	0,017	0,009	-0,260	-22,0	42,2	24,3
					-22,7	-13,4	-13,2	-31,8	36,4	50,6	0,08	0,580	-0,260	-54,0	38,6	65,2
	T10	1,9921	1,9965	2,0023	-48,8	-48,4	-72,8	-173,4	19,4	176,7	-0,17	0,200	-0,030	-6,0	9,5	11,5
					-47,7	-47,4	-73,0	2,8	22,0	-2,1	-0,17	0,200	-0,030	114,0	4,0	-108,0
	Cd	T7	1,9801	1,9880	2,0022	-38,5	-38,3	-58,9	-1,4	17,6	-2,2	-0,17	0,200	-0,030	-24,8	9,1
-37,6						-37,4	59,0	175,1	18,3	-173,5	-0,17	0,200	-0,030	173,0	12,0	173,0
T8		1,9861	1,9903	2,0022	-36,5	-36,4	-61,0	-6,9	28,5	-14,5	0,19	-0,160	-0,030	11,3	32,5	-50,0
					-36,6	-23,5	-23,4	29,2	41,9	-38,2	0,044	0,200	-0,240	48,0	41,0	-52,0
					-13,4	-20,4	-13,2	45,6	40,7	-25,3	0,19	0,070	-0,260	29,0	45,0	-13,0
					-6,1	-6,0	-15,2	171,1	27,3	-134,7	-0,19	0,140	0,050	79,0	16,0	-97,0
T10		1,9889	1,9924	2,0023	-31,3	-31,2	-48,5	-73,5	15,3	72,9	-0,18	0,200	-0,020	-140,0	25,0	-176,0
					-24,0	-24,1	-43,7	-156,3	40,1	161,7	-0,16	0,150	0,010	-161,0	22,0	169,0
					-17,5	-10,6	-10,7	-163,3	15,5	158,5	0,09	-0,260	0,170	-172,0	23,0	174,0
					-8,0	-15,3	-8,1	-72,1	15,9	117,1	-0,26	0,080	0,180	-70,0	22,0	114,0
					-5,0	-9,7	-5,1	-163,2	37,5	170,1	-0,27	0,110	0,160	161,0	34,0	-150,0

S2. Experimental and computational details

S2.1 Sample preparation and ^{17}O enrichment

The H-ZSM-5 zeolite (commercial sample CBV8014, supplied by Zeolyst, Si/Al = 40) was dehydrated by thermal treatment at 673 K under dynamic vacuum (residual pressure $<10^{-4}$ mbar) for two hours and subsequently calcined at 773 K in O_2 atmosphere to remove spurious organic residues.

Framework substitution of ^{16}O by ^{17}O was obtained by heating the dehydrated H-ZSM5 at 120 °C for 2 h, in presence of H_2^{17}O vapors.

Zn- and Cd-loaded ZSM-5 were prepared by in situ sublimation of the metals on the ^{17}O enriched H-ZSM-5 zeolite, following the procedure described in refs.1 and 2. The activated zeolite was exposed for 2 minutes to the metal vapours and subsequently photoirradiated with UV/Vis light with a 1500W xenon lamp (New Port Instruments). The metal content was estimated to be of the order of 2%wt by energy dispersive X-ray spectroscopy (EDS), with a scanning electron microscopy FEI Quanta 200 FEG-ESEM equipped with an EDAX EDS detector.

S2.2 Spectroscopic characterization

X-band (microwave frequency 9.46 GHz) CW EPR spectra were detected at $T = 77$ K and $T = 298$ K on a Bruker EMX spectrometer equipped with a cylindrical cavity. A modulation frequency of 100 kHz, a modulation amplitude of 0.2 mT, and a microwave power of 0.02 mW were used. X-band (microwave frequency 9.76 GHz) and Q-band (microwave frequency 33.7 GHz) pulse EPR experiments were carried out at $T = 50$ K and $T = 298$ K on a Bruker ELEXYS 580 EPR spectrometer, equipped with helium gas-flow cryostat from Oxford Inc. The magnetic field was measured with a Bruker ER035M NMR gaussmeter.

Electron-spin-echo (ESE) detected EPR spectra were recorded with the pulse sequence $\pi/2-\tau-\pi-\tau$ -echo. Pulse lengths $t_{\pi/2} = 16$ ns and $t_{\pi} = 32$ ns, a τ value of 200 ns and a 0.5 kHz shot repetition rate were used.

Q-band Hyperfine Sublevel Correlation (HYSCORE) ³ experiments were carried out with the pulse sequence $\pi/2-\tau-\pi/2-t_1-\pi-t_2-\pi/2-\tau$ -echo, applying a eight-step phase cycle for eliminating unwanted echoes. Microwave pulse lengths $t_{\pi/2} = 16$ ns, $t_{\pi} = 32$ ns, and a shot repetition rate of 0.5 kHz were used. The t_1 and t_2 time intervals were incremented in steps of 8 ns, starting from 200 ns giving a data matrix of 250 x 250 points. The time traces of the HYSCORE spectra were baseline corrected with a third-order polynomial, apodized with a Hamming window and zero filled. After two-dimensional Fourier transformation, the absolute value spectra were calculated. Spectra with different τ values were recorded, which are specified in the figure captions. The spectra were added for the different τ values in order to eliminate blind-spot effects. All EPR spectra were simulated employing the Easyspin package. ⁴

S2.3 Computational details

The ZSM-5 periodic models were built starting from the siliceous Silicalite-1 MFI structure as refined by Artioli and coworkers ⁵ by replacing a single Si atom by an Al one. The charge mismatch due to substitution was initially balanced by adding a proton (i.e. simulating the zeolite in its protonic form). At high Si/Al ratios (as in the case of a single substitution), the MFI framework has P21/n symmetry, thus its unit cell contains 24 crystallographic independent substitutional sites for heteroatoms (i.e. Al).⁶ Upon the single atom substitution, the symmetry of the systems is removed: all the calculation described hereafter refers to P1 models. Since a computational demanding pre-screening of the relative stability of the 24 sites falls outside the scope of this work, some representative cases have been selected on the basis of previous literature. In particular, diffraction studies on Cs substituted ZSM-5 highlighted as preferential substitution occurs at some specific sites:⁷ beside some discrepancies, sites T7, T8 and T10 are generally more favorably substituted. These particular sites, despite being positioned on the same pentasyl building unit, present the further advantage of showing slightly different local environments, as showed in Figure S2.

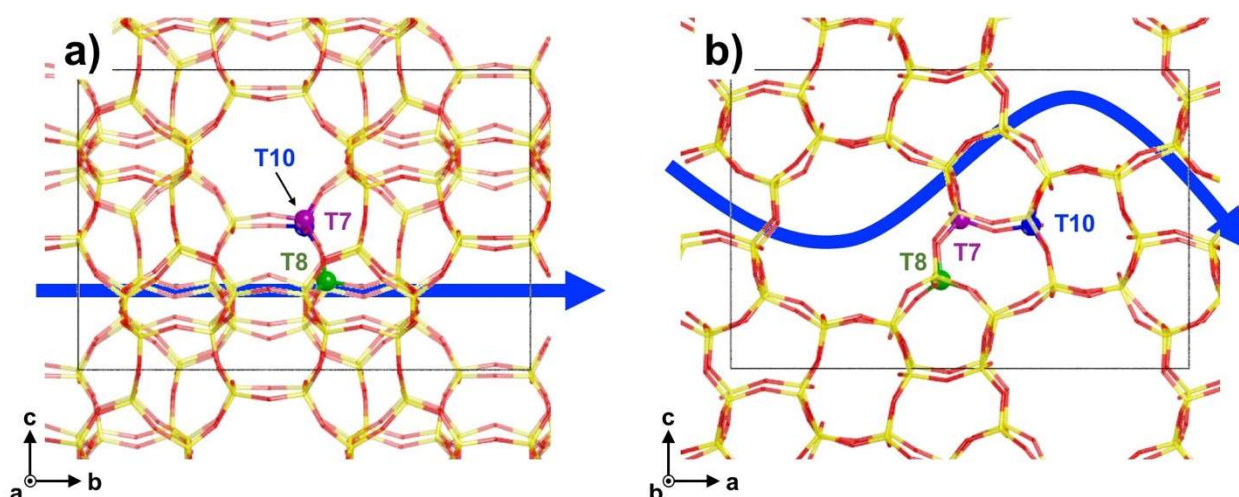


Figure S2 Positioning of sites T7, T8 and T10 in the MFI structure, viewed along the *a* (a) and *b* (b) axes. The blue arrows highlight the sinusoidal and the straight channels, running along the *a* and *b* axes respectively.

Site T7 is exposed at the crossing of the sinusoidal and the straight channels, running along the *a* and the *b* channel respectively, thus it can host the charge balancing cations in the intersection cavity. Site T8 is placed on the wall of the straight channel, with a relatively flat local environment. Conversely, site T10 is positioned on a step of the sinusoidal channel, surrounded by a more heterogeneous environment.

The H-ZSM-5 models generated from substitution of Si by Al at sites T7, T8 and T10 were preliminary relaxed, then the proton was replaced by Zn⁺ or Cd⁺ cations and relaxed again to yield the structural model for the calculation of observables to be compared with experimental results. The geometrical parameters of the relaxed models are reported in Table S2. The corresponding structures are available for downloading in .cif format.

Table S2 Cell parameters (*a*, *b*, *c*), angles (*α*, *β*, *γ*) and volume (*V*) for the nine relaxed periodic models adopted in this study. Distances are expressed in Å, angles in °, volume in Å³.

Site		<i>A</i>	<i>b</i>	<i>b</i>	<i>α</i>	<i>β</i>	<i>γ</i>	<i>V</i>
T7	H ⁺	19.691	19.978	13.355	90.3	91.4	90.1	5252
	Zn ⁺	19.694	19.961	13.350	90.2	91.3	90.1	5246
	Cd ⁺	19.688	19.959	13.352	90.2	91.3	90.2	5245
T8	H ⁺	19.683	19.977	13.347	90.4	91.4	90.0	5246
	Zn ⁺	19.701	19.945	13.344	90.5	91.3	90.1	5241
	Cd ⁺	19.693	19.936	13.347	90.5	91.3	90.1	5238
T10	H ⁺	19.709	20.003	13.333	89.7	91.4	89.9	5254
	Zn ⁺	19.683	20.012	13.337	89.7	91.5	89.9	5251
	Cd ⁺	19.676	19.971	13.328	90.0	91.3	89.9	5235

In order to qualitatively infer the relative population of the three sites upon substitution of the Brønsted proton by Zn⁺/Cd⁺, the following reaction has been simulated:



where Z is the zeolite framework and M = Zn or Cd. The electronic energy of reaction was calculated accordingly as follows:

$$\Delta E = E(M^+Z) + \frac{1}{2} E(H_2) - E(H^+Z) - E(M) \quad (2)$$

Finally, the relative population of sites (at STP conditions) was estimated through the Boltzmann distribution:

$$p_{T_i} = \frac{\exp\left(\frac{-\Delta E_{T_i}}{RT}\right)}{\sum \exp\left(\frac{-\Delta E_{T_i}}{RT}\right)} \quad (3)$$

with $T_i = T7, T8$ or $T10$. The results from eq. 2 and 3, for both Zn and Cd substitutions, are summarized in Table S3.

Table S3 Electronic reaction energies (ΔE , expressed in kJmol^{-1}) and relative site population of sites T7, T8 and T10 upon substitution by Zn^+/Cd^+ .

	Site	ΔE	p_{T_i}
Zn	T7	-47.4	0.33
	T8	-37.1	0.01
	T10	-49.2	0.67
Cd	T7	-60.6	0.01
	T8	-68.3	0.27
	T10	-70.7	0.72

The periodic calculations (geometry relaxations and isotropic and anisotropic hyperfine couplings estimations) have been performed with the CRYSTAL17 code, by exploiting the B3LYP hybrid functional.^{8,9} Dispersive interaction, that could have a relevant effect in determining geometry and adsorptive properties of zeolites,¹⁰ have been included empirically through the Grimme D2 scheme.¹¹ Concerning the basis set, since electronic properties have been computed, a rich, all-electron base would be preferable. However, since the localized nature of the properties investigated, i.e. limited to atoms close to the spin-polarized one, sufficiently far species can be described with lower quality bases without affecting significantly the accuracy of the calculations.¹² Thereby, only atoms sufficiently close to Zn^+/Cd^+ (distance $< 4 \text{ \AA}$) have been described through the Ahlrichs TZV2p basis set.¹³ Concerning the extraframework cations, H^+ and Zn^+ have been described through the Ahlrichs TZV2p too, whereas the TZV basis set from Campos et al. (pruning the g basis functions, as not yet implemented in CRYSTAL) has been used for Cd^+ .¹⁴ The remaining framework atoms have been described through the double- ζ quality basis set proposed by Nada and coworkers,¹⁵ proved to give a proper description of zeolite models at a reasonable computational cost. All the basis sets adopted in the calculation are reported (in the CRYSTAL format) in section S6. The truncations for the mono- and bi-electronic integral (TOLINTEG) were set to {7 7 7 25}. The sampling in the reciprocal space (SHRINK) was set to {2 2}, for a total of 8 k points. The maximum order of shell multipoles in the long-range zone for the electron-electron Coulomb interaction (POLEORDR keyword) was chosen to be 6. The spin multiplicity of the wavefunction of metal-substituted models was locked to doublet through the SPINLOCK keyword: the constrain was removed after SCF energy drop below 10^{-6} hartree. All the other parameters were set to default values according to the CRYSTAL17 manual.¹⁶

The experimental observables (g tensor, A and Q tensors for the most relevant atoms and their mutual orientations) were computed through a cluster approach using the ORCA (v4.1.2) code.¹⁷ The cluster models for each cation/site have been straightforwardly derived from the periodic ones by keeping the atoms described through the high-level basis set (i.e. TZV2p). The dangling bonds on Si atoms were saturated by H,

placed at 1.45 Å along the direction of the pristine Si-O bond. The terminal H atoms were also described through the Ahlrichs TZV2p basis set. Such cluster models are graphically presented in Figure S3.

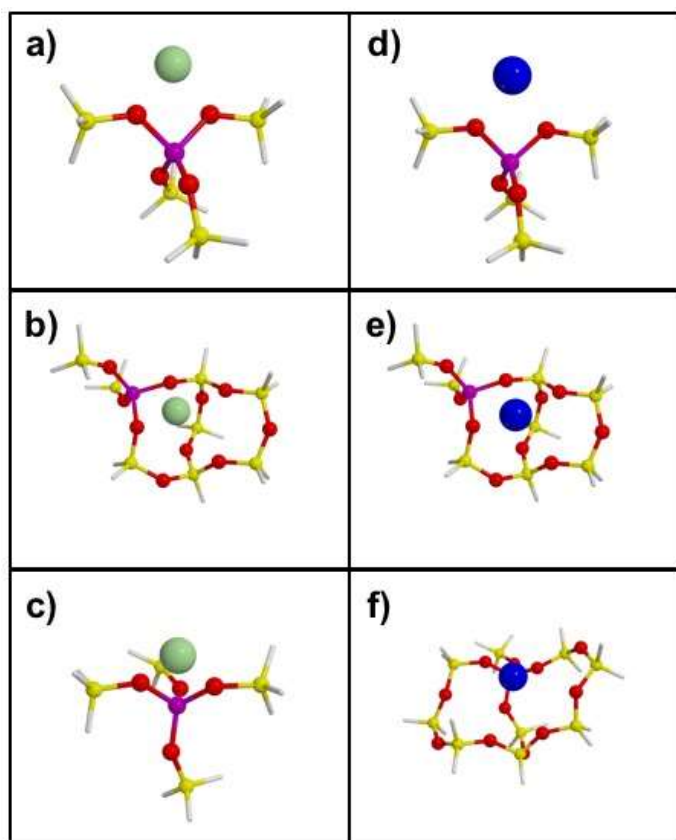


Figure S3 Cluster models exploited in the g tensor calculations: Zn⁺ (a) to c) and Cd⁺ (d) to f) for the three different T sites T7 (a) and d), T8 (b) and e)) and T10 (c) and f)). Atoms color code: green Zn, blue Cd, purple Al, red O, yellow Si). The hydrogen terminations are represented by grey sticks.

The clusters were exploited in the calculation of the g tensors without further geometry relaxation, retaining the same level of theory for the periodic calculation (B3LYP-D2). The EPR hyperfine tensor elements of ¹⁷O appear to be systematically overestimated, in particular the a_{iso} term. This quantity is hard to reproduce quantitatively due to the need to describe with great accuracy the Fermi contact term, which in turn depends on the description of the core orbitals of the system. Moreover, the computed a_{iso} is known to be very sensitive to the exchange functional employed. To check this, calculations have been repeated with the BHandHLYP functional for one of the considered sites (T7). Indeed a reduction in the ¹⁷O computed hfi is observed in this case (Table S4). These differences however do not change the overall picture and for internal consistency, only B3LYP periodic (CRYSTAL) and molecular (ORCA) results will be discussed.

Table S4. Comparison of DFT computed ¹⁷O hfi tensor elements (in MHz) using B3LYP and BHandHLYP functionals.

	17O A tensor				17O Euler rotation (A to g)			17O Quadrupole tensor	
	a iso	Ax	Ay	Az	Alpha	Beta	Gamma	e**2qQ	eta
BHandHLYP	-58,4	6,8	6,6	-13,4	0,7	19,1	-1,8	4,124	0,103
B3LYP	-60,8	7,8	8,1	-15,8	1,0	19,0	-1,8	4,170	0,758
BHandHLYP	-58,2	7,0	6,9	-13,9	179,7	19,5	-176,5	4,038	0,779
B3LYP	-60,2	8,2	8,4	-16,6	174,0	19,5	-174,4	4,093	0,718

S3. Determination of acid sites density of the parent and the steamed samples

The exposure of acid zeolites to water vapors at high temperature (i.e. steaming) is known to possibly cause the leaching of the framework Al to extraframework positions, consequently losing its charge balancing Brønsted acid proton, in a process referred as dealumination.¹⁸ The extent of the dealumination depends on the steaming temperature, as well as on the time of treatment. The newly formed extraframework Al is characterized by a significant Lewis acidity, thus a way to assess the occurrence of dealumination is to quantify the population of Brønsted and Lewis sites in the zeolite before and after the steaming. A convenient method, allowing quantification both the families of acid sites at once, is the IR spectroscopy of adsorbed pyridine: several literature reports developed and/or exploited such methodology,¹⁹ which is nowadays well established.

Since the framework substitution of ¹⁶O by ¹⁷O relies on a mild steaming (120 °C for 2 h, in presence of H₂¹⁷O vapors), we verified whether such treatment could lead to dealumination of the framework. A self-supported pellet of H-ZSM-5 was preliminary activated at high temperature (500 °C) in high vacuum (residual pressure < 10⁻⁴ mbar), thus exposed at RT to the pyridine vapor pressure for 30 min. The excess of physisorbed pyridine was thus eliminated by 1 h of outgassing at RT, followed by 1 h of outgassing at 200 °C. After cooling, an IR spectrum was collected with a Bruker Vertex 70 FT-IR spectrometer, equipped with a MCT detector, by accumulating 32 scans at 2 cm⁻¹ resolution. Such spectrum was exploited in the quantification of the acid sites for the “as such” sample. Another self-supported pellet of H-ZSM-5, preliminary activated as described above, was then heated back to 120 °C and consequently exposed to the vapor pressure of water (H₂¹⁶O, avoiding to use of expensive H₂¹⁷O) and kept under these conditions for 2 h. At the end of the steaming, water vapors were outgassed and the temperature was increased again to 500 °C, in order to fully dehydrate the material for the subsequent interaction with pyridine. Pyridine was dosed and partly desorbed following the same scheme as for the “as such” sample. Finally, the IR spectrum of the “steamed” sample was collected for the sake of quantification. The spectra used for the quantification are presented in Figure S4.

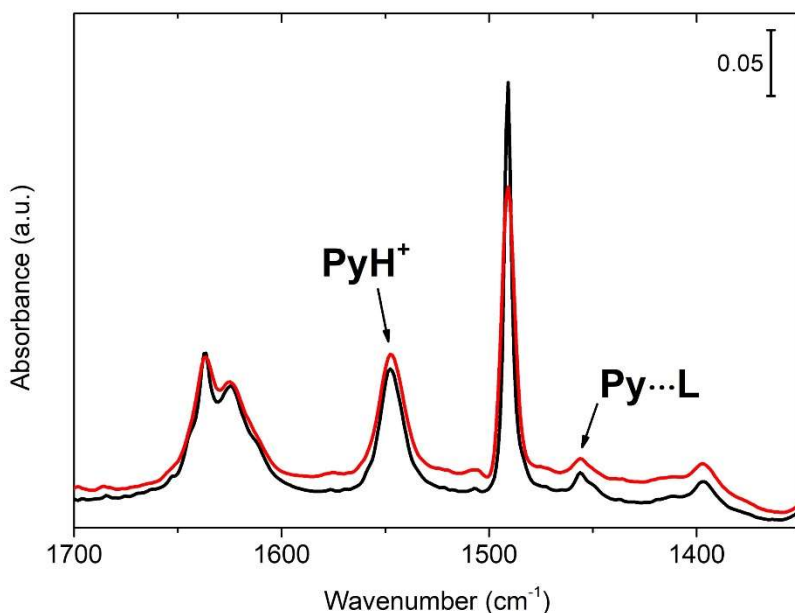


Figure S4. IR spectra of the bare (black curve) and steamed (red curve) H-ZSM-5, contacted with pyridine and thus outgassed at 200 °C for 1 h. The bands exploited for the Brønsted (PyH⁺) and Lewis (Py...L) sites quantification are labeled in the figure.

The quantification procedure accounts on the integrated area (determined through the FIT routine of the Opus software) of the bands associated to the perturbed 19b ring mode of pyridine adsorbed on Brønsted

(PyH⁺ 1545 cm⁻¹) and Lewis (Py···L 1455 cm⁻¹) acid sites.²⁰ The integrated area values were normalized to the surface density of each self-supported pellet (expressed in g/cm²) and the quantification of the sites was achieved by exploiting the molar extinction coefficients proposed by Datka et al.¹⁹

The results of the acid sites quantification for both samples are reported in Table S5.

Table S5 Acid sites density determined by IR spectroscopy of adsorbed pyridine (expressed in μmol/g) of the parent H-ZSM-5, as such and steamed by H₂¹⁶O vapors (5 mbar) at 120 °C for 2 h.

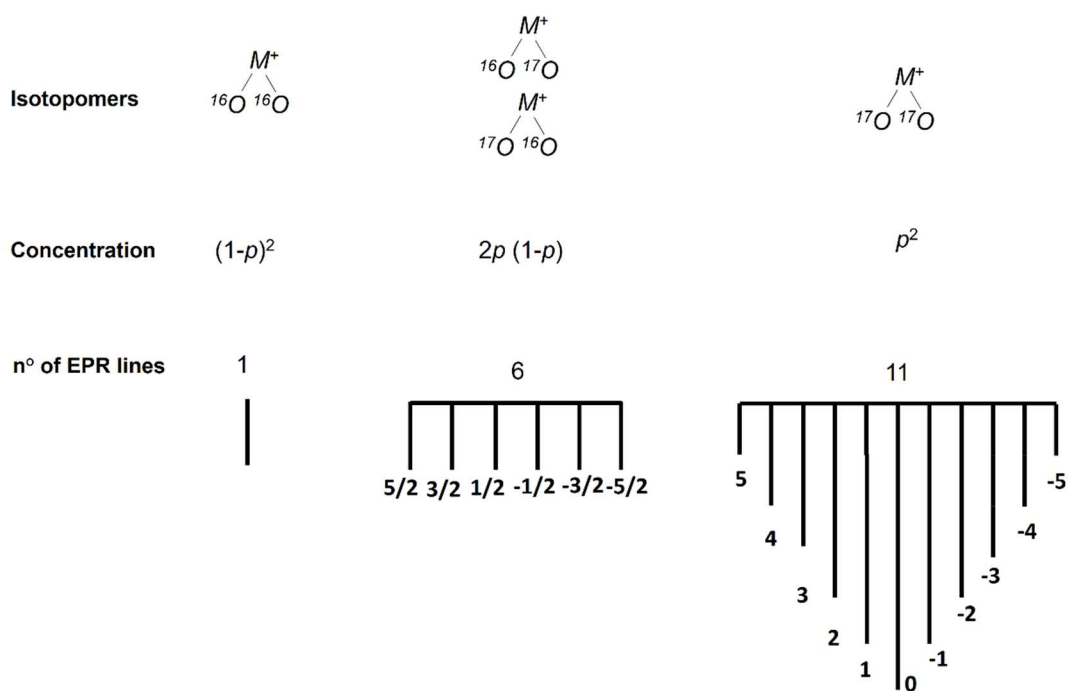
	Brønsted	Lewis	Total
As such	361	22	383
Steamed	353	25	378

As Table S5 demonstrates, the mild steaming conditions adopted in this work does not significantly affect the nature of the acid sites in the steamed material with respect to the untreated one.

S4. EPR Spectra Simulation

S4.1 Simulation of the CW-EPR spectra

The EPR spectra of paramagnetic metal ions in ZSM-5 zeolites are generally characterized by the presence of multiple species reflecting different binding sites. In the case of Zn⁺ in the unlabeled zeolite, the EPR spectrum can be satisfactorily simulated assuming a single species. This is in good agreement with the results of the DFT calculations, which show that no significant difference is observed in the **g** tensor of the two potential adsorption sites (T7 and T10, see Table 2 of the main text). Under these circumstances, in the case of the ¹⁷O enriched sample, the *hfi* structure observed in the CW spectra (Figure 1 of the main text, Figure S5 and Figure S6), must arise from the superposition of several sub-spectra, arising from various isotopomers. In particular, considering only the two strongly coupled oxygens (Figure 3 of the main text), the following three isotopomers (¹⁶O-¹⁶O), (¹⁷O-¹⁶O) and (¹⁷O-¹⁷O) can be considered, whose relative abundance will depend on the level of isotopic enrichment. The relative abundance P^{nn} of such isotopomers is given by $P^{16-16} = (1 - p)^2$, $P^{16-17} = 2p(1 - p)$ and $P^{17-17} = p^2$, where p is the ¹⁷O enrichment level. The number of lines and the abundance of the oxygen isotopomers are summarized in the following scheme, where for the doubly labeled (¹⁷O ¹⁷O) species, a total nuclear spin number $I = I_1 + I_2 (5/2 + 5/2 = 5)$ is used to label the hyperfine transitions. Because the nuclear magnetic moment of ¹⁷O is negative ($g_0 = -0.75752$), the successive hyperfine satellites appearing with increasing magnetic field are transitions from $m_I = 5/2$ to $m_I = -5/2$, for singly labeled species, and from $m_I = 5$ to $m_I = -5$ for doubly labeled species, respectively.



Scheme S1 Number of EPR lines and abundance of the oxygen isotopomers for a representative site involving two oxygen nuclei.

Given the complexity of the system, the simulation strategy was to use the *hfi* tensor obtained from the analysis of the ^{17}O HYSCORE spectra and the *g* tensor obtained from the simulation of the unlabeled system. In the ^{17}O HYSCORE spectrum (Figure S7) we observe a pair of cross peaks in the (-,+) quadrant corresponding to a *hfi* tensor $\mathbf{A}=[47\ 47\ -62]$ MHz (vide infra). These couplings are in line with those predicted from DFT (Table 2 of the main text) for the directly coordinated oxygens and have been used for the simulation while no attempts was made to include the small ^{17}O *hfi* couplings detected in the HYSCORE (+,+) quadrant and the ^{27}Al couplings. A simulation analysis was then performed based on the different relative abundance of the three isotopomers, calculated as described above, assuming a level of ^{17}O enrichment of 10%, 50%, 70% and 90%. The line-width of the different contributing species was adjusted based on the best fit of the experimental spectrum and kept fixed in all simulations, so that only the relative abundance of the three isotopomers was left as a free parameter allowed to vary. In this way, a convincing fitting of the experimental spectrum was obtained, which points to a ^{17}O enrichment of the order of $70\pm 10\%$. The results of this simulation analysis are reported in Figure S5 and the spin-Hamiltonian parameters used in the simulation, including the relative abundance of the three isotopomers are reported in Table S6.

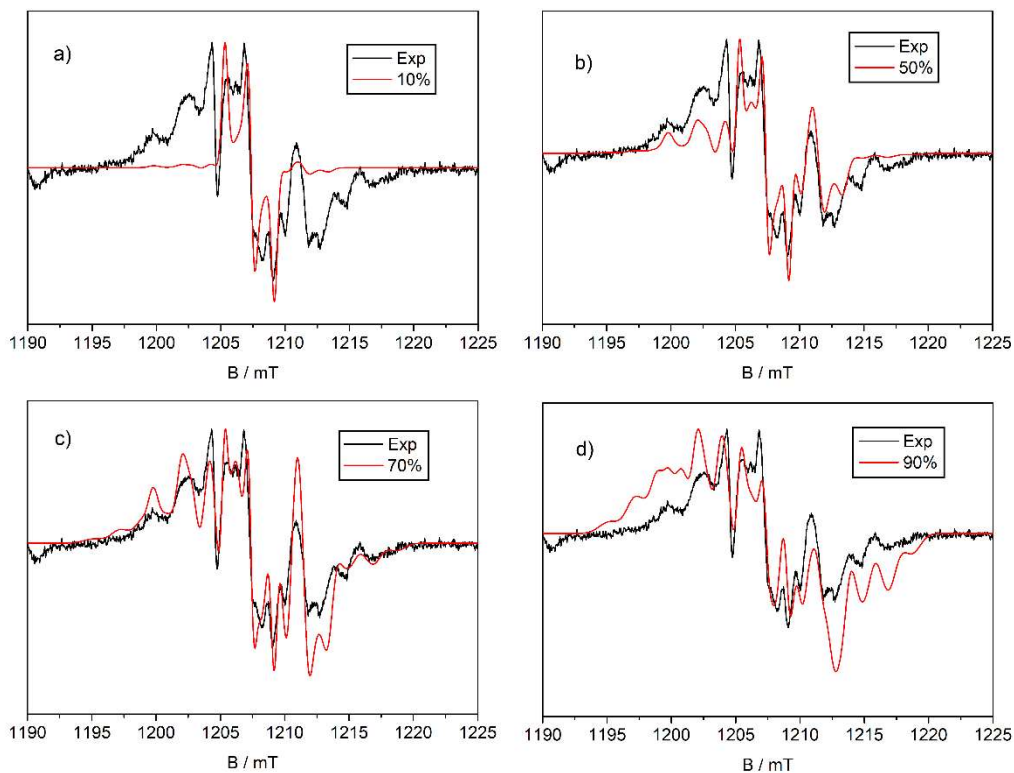


Figure S5 Experimental (black) and simulated (red) Q-band CW EPR spectra of Zn^{2+} ions adsorbed on ^{17}O -ZSM-5.

Table S6 Spin Hamiltonian parameters used in the simulations reported in Figure S6.

Metal	Isotopomer	Abundance	g tensor			$^{17}\text{O}1$ A tensor				$^{17}\text{O}2$ A tensor				$^{17}\text{O}3$ A tensor			
			g_1	g_2	g_3	a_{iso}	T_1	T_2	T_3	a_{iso}	T_1	T_2	T_3	a_{iso}	T_1	T_2	T_3
Zn	16-16	0.09	1.9951	1.9984	2.0015	-	-	-	-	-	-	-	-				
	16-17	0.42	1.9951	1.9984	2.0015	-52	+5	+5	-10								
	17-17	0.49	1.9951	1.9984	2.0015	-52	+5	+5	-10	-52	+5	+5	-10				
Cd	16-16	0.11	1.9891	1.9932	2.0007												
	16-17	0.11	1.9891	1.9932	2.0007	-29	+5	+5	-10								
	16-17	0.11	1.9891	1.9932	2.0007					-40	+5	+5	-10				
	16-17	0.06	1.9891	1.9932	2.0007									-21	+2.5	+2.5	-10
	17-17	0.22	1.9891	1.9932	2.0007	-29	+5	+5	-10	-40	+5	+5	-10				
	17-17	0.17	1.9891	1.9932	2.0007	-29	+5	+5	-10					-21	+2.5	+2.5	-10
	17-17	0.22	1.9891	1.9932	2.0007					-40	+5	+5	-10	-21	+2.5	+2.5	-10

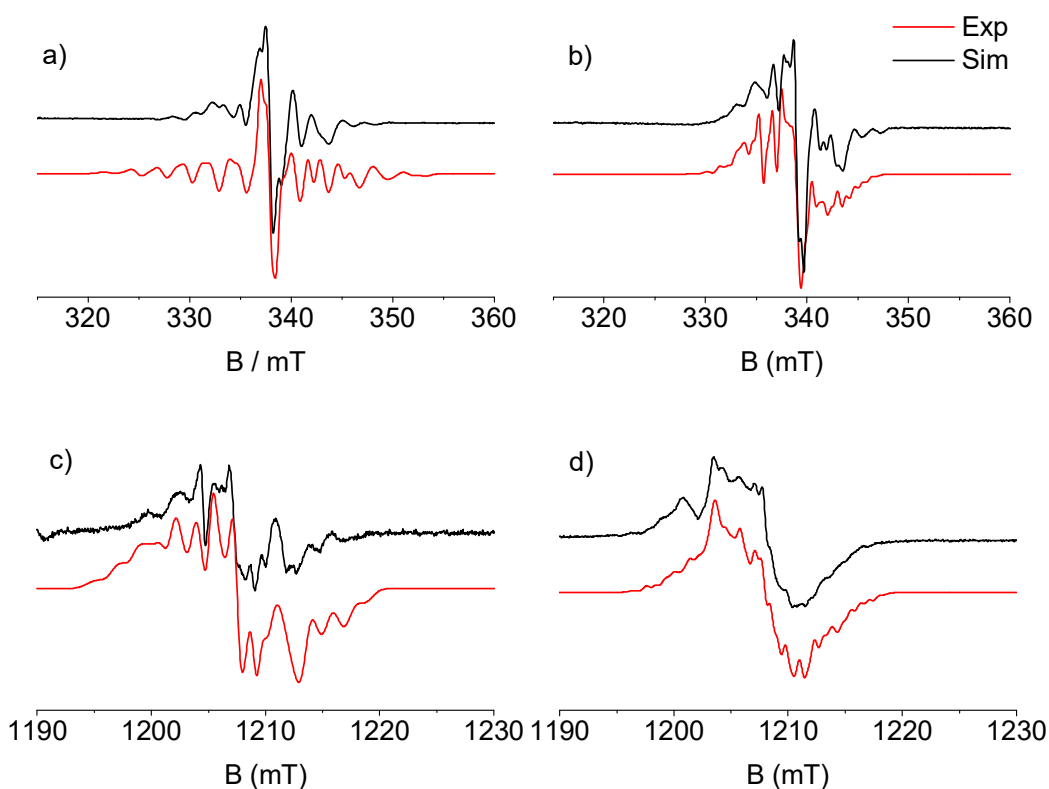


Figure S6 Experimental (black) and simulated (red) CW EPR spectra of Zn⁺ (a,c) and Cd⁺ on ¹⁷O ZSM5 (b,d). Spectra a) and b) were recorded at X band frequency, c) d) at Q band frequency.

S4.2 Characteristics of HYSCORE spectra from $I=5/2$ and HYSCORE simulations.

The most informative experimental data regarding the ligand environment of Zn⁺ and Cd⁺ were obtained from HYSCORE experiments. The basic advantage of the HYSCORE technique is the creation in 2D spectra of off-diagonal cross-peaks whose coordinates are nuclear frequencies from opposite electron spin manifolds. The cross-peaks simplify significantly the analysis of congested spectra by correlating and spreading out the nuclear frequencies. In addition, the HYSCORE experiment separates overlapping peaks along a second dimension and enhances the signal-to-noise ratio through the application of a second Fourier transform.

HYSCORE spectra are sensitive to the relative signs of the correlated frequencies and are usually presented as two quadrants (+,+) and (+,-). ¹⁷O is a $I = 5/2$ nucleus with $g_n = -0.75752$, which means that the two electron spin manifolds α ($m_s = 1/2$) and β ($m_s = -1/2$) will split into six levels according to the nuclear spin quantum numbers, which range from $m_I = 5/2$ to $m_I = -5/2$. In general due to the nuclear quadrupole interaction these levels will be shifted proportionally to $(m_I)^2$. The HYSCORE spectrum for such a system will consist theoretically of $2(2I)^2 = 50$ correlation peaks for the $|\Delta m_I| = 1$ transitions and a number of cross peaks corresponding to $|\Delta m_I| = 2, 3$, etc. Not all these transitions are actually observed and in particular, at Q band frequency we observe ¹⁷O correlation lines in the (++) quadrants, which correspond to transition frequencies of ¹⁷O between the states with the nuclear spin projections $m_I = 1/2$ and $m_I = -1/2$. These are those least affected by the nuclear quadrupole interaction (nqi) and are the most intense ones, and their frequencies are approximately (to first order in hfi and nqi) given by $\nu = \nu_0 \pm A/2$, where ν_0 is the ¹⁷O Zeeman frequency and A is the secular component of the hyperfine interaction. In order to test the effect of the quadrupole

interaction, simulations were carried out using the values determined by DFT computations and compared with simulations obtained without considering the quadrupole interaction. The result indeed indicates that under these circumstances (large isotropic hyperfine components) the effect of the nuclear quadrupole interaction is not clearly resolved at Q band frequency and that the computed values provide a good fit of the experimental data.

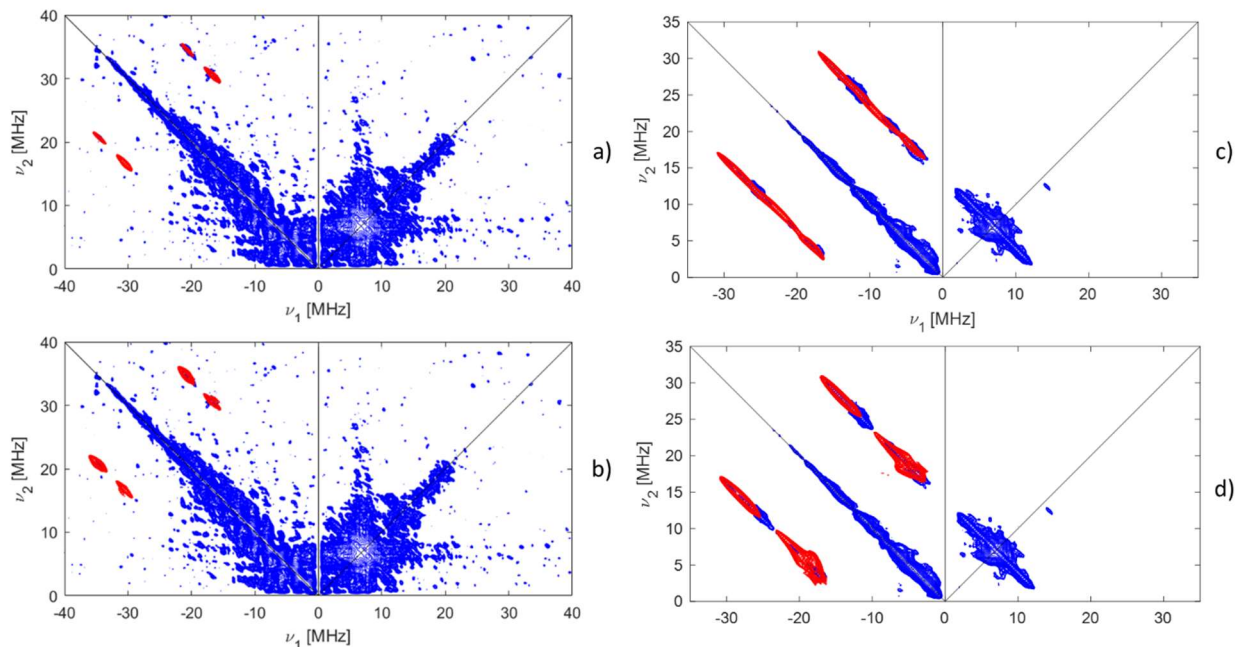


Figure S7 Evaluation of the effect of the nuclear quadrupole interaction in Q-band ^{17}O HYSCORE experiments in Zn (a, b) and Cd (c, d) in ZSM-5. In Figure a) and c) the nuclear quadrupole interaction was neglected, while in Figures b) and d) the values and orientations obtained from DFT computations were used. Specifically the simulation in Figure b) was obtained using the following values: $A = 51 + [-5 \ -5 \ 10]$ MHz (Euler angles $[174 \ 19.5 \ -174]$ degrees) $Q = [-0.17 \ 0.2 \ -0.03]$ MHz (Euler angles $[-15 \ 13 \ 7]$ degrees), while the simulation in Figure d) was obtained with the following set of parameters: $A_1 = 40 + [-5 \ -5 \ 10]$ MHz (Euler angles $[-14 \ 17.6 \ -2.2]$) $Q = [-0.17 \ 0.2 \ -0.03]$ MHz (Euler angles $[-25 \ 9 \ 15]$ degrees), $A_2 = 29 + [-5 \ -5 \ 10]$ MHz (Euler angles $[-156 \ 40 \ 162]$) $Q = [-0.16 \ 0.15 \ 0.01]$ MHz (Euler angles $[-161 \ 22 \ 169]$), $A_3 = 21 + [-2.5 \ -2.5 \ 5]$ MHz (Euler angles $[-163 \ 15 \ 168]$) $Q = [-0.26 \ 0.08 \ 0.18]$ (Euler angles $[-72 \ 23 \ 114]$ degrees).

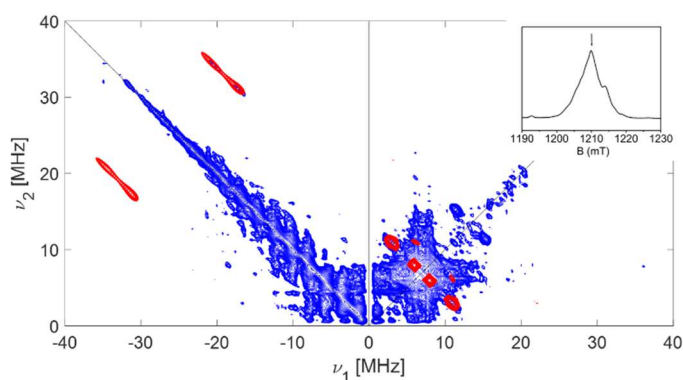


Figure S8 Experimental (blue) and simulated (red) Q band HYSCORE of Zn^{2+} . The spectrum is the result of the sum after Fourier transform of spectra recorded with 2τ values (114 ns and 242 ns)

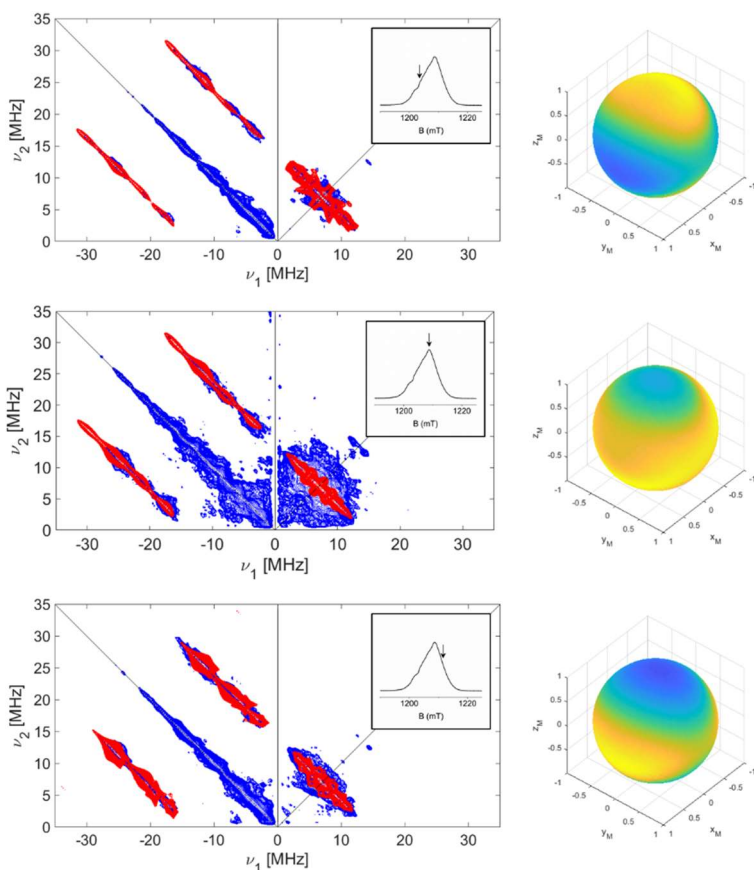


Figure S9 Experimental (blue) and simulated (red) Q band HYSCORE spectra taken at different observer positions. Spectra acquired with different τ values (100 ns, 144 ns and 214 ns) were added together after Fourier transform to avoid blind spot effects. All spectra were recorded at 70 K. In the simulations the relative orientations of the A tensors with respect to g tensor (Euler angles) and nuclear quadrupole tensors obtained by DFT and reported in the caption of Figure S7 were used.

S5. Calculation of spin density from the isotropic and the dipolar parts of the ^{17}O hyperfine couplings.

From the observation of the hyperfine structure and determination of the isotropic (a_{iso}) and dipolar (T) hyperfine couplings, the electronic spin distribution in a molecular fragment can be obtained.²¹ To do so it is important that the hf interaction with several (preferably all!) nuclei in the molecule are observed. Then, with the knowledge of a_{iso} and T for the atomic species, and assuming that the hf interaction at a given nucleus is proportional to the electron spin density at that nucleus, one can obtain the spin population in s -type orbitals ρ_s , p -type orbitals ρ_p .

For an unpaired electron (free electron, $g_e=2.0023$) on a ^{17}O -nucleus with a unitary spin population ($\rho_s=1$) in an s -type orbital, one would observe an isotropic hyperfine coupling constant of $a_0=3777$ MHz. If the electron resides in a p -type orbital one would observe a uniaxial hyperfine constant of $b_0=107.3$ MHz.²² Including a correction for the difference in the g values, the spin populations in s -type and p -type orbitals can thus be estimated as:

$$\rho_s = \frac{A_{\text{iso}} g_e}{a_0 g_{\text{iso}}}; \rho_p = \frac{T g_e}{b_0 g_{\text{iso}}}$$

In the calculation of ρ_p we remind that the value used for T should be corrected for the through space dipolar interaction between the magnetic moment of ^{17}O and spin population that is located on the metal center. Using the values obtained from the DFT calculations, we can estimate the contribution to the ^{17}O -hyperfine matrix as $\mathbf{T}=[-2.7, -2.7, 5.4]$ MHz and $\mathbf{T}=[-2.1, -2.1, 4.2]$ MHz for Zn^+ and Cd^+ respectively. The corrected value

to estimate ρ_p is thus given by: $T=T_{\text{tot}}-T_{M^+}= 5 \text{ MHz}-2.7 \text{ MHz}=2.3 \text{ MHz}$ for Zn and $T=T_{\text{tot}}-T_{M^+}= 5 \text{ MHz}-2.1 \text{ MHz}=2.3 \text{ MHz}$ for Cd, corresponding to 2.1% p character for the Zn and 2.7% character for Cd.

These values, nicely agrees with the Mulliken spin population reported in Table S7 in particular for sites T7.

Table S7 Mulliken spin population analysis

	Site	d(Zn-O)	Mulliken spin population			
			2px	2py	2pz	
Zn	T7	2,086	0,002	0,021	0,000	
		2,099	0,000	0,020	0,004	
	T8	2,133	0,012	0,019	0,001	
		2,231	0,008	0,004	0,009	
		2,781	0,000	0,002	0,005	
		3,182	0,001	0,002	0,000	
	T10	2,092	0,013	0,012	0,000	
		2,114	0,002	0,024	0,001	
			d(Cd-O)			
	Cd	T7	2,32	0,001	0,009	0,015
2,34			0,000	0,000	0,027	
T8		2,384	0,012	0,016	0,003	
		2,656	0,000	0,000	0,010	
		3,001	0,002	0,002	0,001	
		2,669	0,002	0,000	0,009	
T10		2,405	0,002	0,000	0,017	
		2,603	0,002	0,002	0,021	
		3,114	0,003	0,001	0,000	
		3,089	0,000	0,004	0,000	
		3,25	0,000	0,003	0,000	

S6. Bader Analysis of the electron density distribution

The topological analysis of the electron density distribution and the evaluation of the critical points for the different structures, performed on the periodic models through the TOPOND package embedded in CRYSTAL17, is reported in Figure S8. The critical points are locations where the gradient of the electron density is zero and allow the identification of bond paths.²³ We found that the bond paths depend not only on the specific site considered but also from the metal cation. For site T7 two critical point between both Zn⁺ and Cd⁺ and two Si-O-Al framework oxygens are observed. The T8 site behaves similarly to the former, and four critical points are found: two shorter ones involve the Zn⁺/Cd⁺ and the Si-O-Al oxygen, whereas two longer ones are found between the cation and the oxygen of a siloxane bridge. Conversely, in the case of T10 significantly different bond paths are obtained for the two metals. While Zn⁺ presents a situation analogous to that observed for T7, Cd⁺ shows a bonding interaction with 5 oxygens, including both Al-O-Si and Si-O-Si bridging oxygens. These results are in agreement with the richness of the ¹⁷O HYSORE spectra (particularly in the case of Cd) and point to a non-negligible reactivity of the Si-O-Si bridging oxygens, even under the mild reaction conditions adopted in this work.

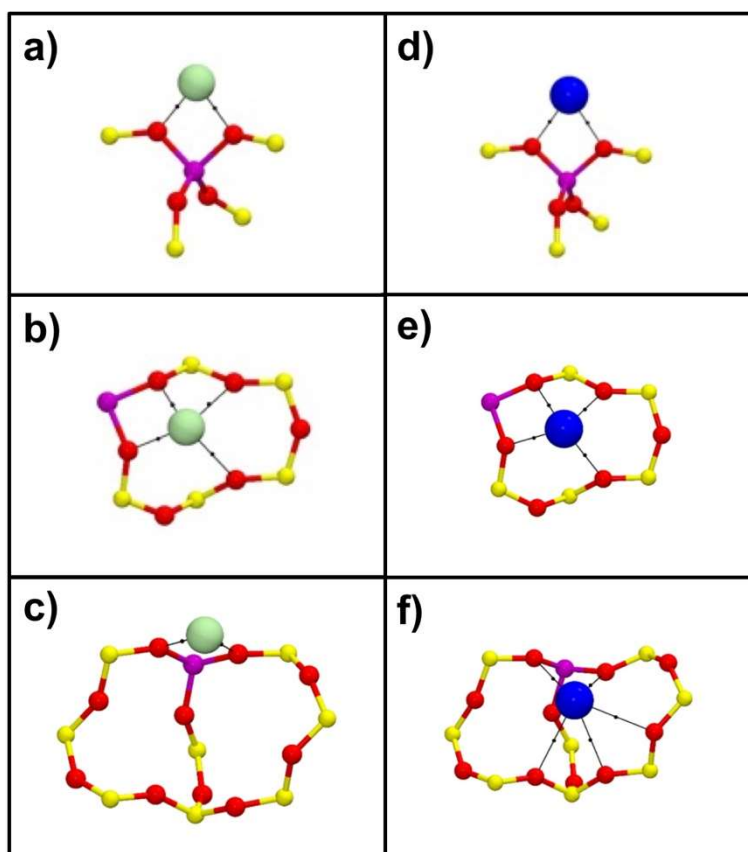


Figure S9 Bader analysis for Zn^+ (a) to c)) and Cd^+ (d) to f)) for the three different T sites T7 (a) and d), T8 (b) and e)) and T10 (c) and f)). The critical points of the electron density for each model are represented by the black dots. Atoms color code: green Zn, blue Cd, purple Al, red O, yellow Si).

S7. Basis sets adopted in the calculations (CRYSTAL format)

- **H**

```
1      3
0 0 3 0.0 1.0
34.0613410  0.60251978E-02
5.1235746   0.45021094E-01
1.1646626   0.20189726
0 0 1 0.0 1.0
0.32723041  1.0
0 0 1 0.0 1.0
0.10307241  1.0
```

- **O (low-level)**

```
8      5
0 0 8 2.0 1.0
8966.29     0.001
1240.17     0.0091
252.114     0.0513
70.359      0.1702
23.9025     0.3662
9.2075      0.3859
3.9847      0.1471
1.2266      0.0695
0 1 4 8.0 1.0
44.9344     -0.0098 0.0107
10.3978     -0.0893 0.067
3.297       -0.0373 0.21
1.234       0.373  0.3542
0 1 1 0.0 1.0
0.4536      1.0    1.0
0 1 1 0.0 1.0
0.181       1.0    1.0
0 3 1 0.0 1.0
0.6         1.0
```

- **O (high-level)**

```
8      10
0 0 6 2.0 1.0
27032.3826310 0.21726302465E-03
4052.3871392  0.16838662199E-02
922.32722710 0.87395616265E-02
261.24070989 0.35239968808E-01
85.354641351 0.11153519115
31.035035245 0.25588953961
0 0 2 2.0 1.0
12.260860728 0.39768730901
4.9987076005 0.24627849430
0 0 1 0.0 1.0
```

1.1703108158 1.0
0 0 1 0.0 1.0
0.46474740994 1.0
0 0 1 0.0 1.0
0.18504536357 1.0
0 2 4 6.0 1.0
63.274954801 0.60685103418E-02
14.627049379 0.41912575824E-01
4.4501223456 0.16153841088
1.5275799647 0.35706951311
0 2 1 0.0 1.0
0.52935117943 1.0
0 2 1 0.0 1.0
0.17478421270 1.0
0 3 1 0.0 1.0
2.4 1.0
0 3 1 0.0 1.0
0.60 1.0

• **AI**

13 11
0 0 7 2.0 1.0
37792.550772 0.57047888709E-03
5668.0682165 0.44093016538E-02
1289.8582841 0.22630967411E-01
364.86596028 0.88025644295E-01
118.57631515 0.25223701612
42.024867605 0.45960547169
15.499501629 0.33277886014
0 0 3 2.0 1.0
75.208026598 0.19250560190E-01
23.031408972 0.87906743952E-01
3.6348797649 -0.34246704535
0 0 2 0.0 1.0
1.6065049957 1.5106266058
0.76103394581 0.58071016470
0 0 1 0.0 1.0
0.16556708849 1.0
0 0 1 0.0 1.0
0.060041577113 1.0
0 2 6 6.0 1.0
452.52303192 0.23110812466E-02
107.08195049 0.18568641823E-01
34.131021255 0.87216237035E-01
12.587037428 0.26902101523
4.9811919704 0.52128324272
2.0070350900 0.60271687494
0 2 1 0.0 1.0
0.80083714374 1.0
0 2 1 0.0 1.0
0.20178927472 1.0
0 2 1 0.0 1.0

0.057895550392 1.0
0 3 1 0.0 1.0
0.6 1.0
0 3 1 0.0 1.0
0.15 1.0

• **Si (low-level)**

14 5
0 0 8 2.0 1.0
149866.0 0.0001215
22080.6 0.0009770
4817.5 0.0055181
1273.5 0.0252000
385.11 0.0926563
128.429 0.2608729
45.4475 0.4637538
16.2589 0.2952000
0 1 8 8.0 1.0
881.111 -0.0003 0.0006809
205.84 -0.0050 0.0059446
64.8552 -0.0368 0.0312000
23.9 -0.1079 0.1084000
10.001 0.0134 0.2378000
4.4722 0.3675 0.3560066
2.034 0.5685 0.3410000
0.9079 0.2065 0.1326000
0 1 3 0.0 1.0
2.6668 -0.0491 0.0465000
1.0780 -0.1167 -0.1005000
0.3682 0.2300 -1.0329000
0 1 1 0.0 1.0
0.193 1.0 1.0
0 3 1 0. 1.
0.610 1.0

• **Si (high-level)**

14 11
0 0 7 2.0 1.0
44773.3580780 0.55914765868E-03
6717.1992104 0.43206040189E-02
1528.8960325 0.22187096460E-01
432.54746585 0.86489249116E-01
140.61505226 0.24939889716
49.857636724 0.46017197366
18.434974885 0.34250236575
0 0 3 2.0 1.0
86.533886111 0.21300063007E-01
26.624606846 0.94676139318E-01
4.4953057159 -0.32616264859
0 0 2 0.0 1.0
2.1035045710 1.3980803850
1.0106094922 0.63865786699

0 0 1 0.0 1.0	
0.23701751489	1.0
0 0 1 0.0 1.0	
0.085703405362	1.0
0 2 6 6.0 1.0	
394.47503628	0.26285693959E-02
93.137683104	0.20556257749E-01
29.519608742	0.92070262801E-01
10.781663791	0.25565889739
4.1626574778	0.42111707185
1.6247972989	0.34401746318
0 2 1 0.0 1.0	
0.54306660493	1.0
0 2 1 0.0 1.0	
0.20582073956	1.0
0 2 1 0.0 1.0	
0.070053487306	1.0
0 3 1 0.0 1.0	
0.7	1.0
0 3 1 0.0 1.0	
0.175	1.0
• Zn	
30 14	
0 0 8 2.0 1.0	
405924.3102800	0.22442017483E-03
60846.9557350	0.17402086626E-02
13847.3430920	0.90513339565E-02
3919.6158551	0.36817341445E-01
1276.3594167	0.12004850256
458.67254435	0.28576057621
178.28725246	0.41087462062
70.612192837	0.21816962456
0 0 4 2.0 1.0	
443.88077950	-0.24934274984E-01
137.55875267	-0.11817955766
22.268083479	0.55367318468
9.5217310606	0.52628934936
0 0 2 2.0 1.0	
14.874114065	-0.22929955254
2.4647517612	0.71135484742
0 0 1 1.0 1.0	
1.0113272238	1.0
0 0 1 0.0 1.0	
0.14919852089	1.0
0 0 1 0.0 1.0	
0.051441872981	1.0
0 2 6 6.0 1.0	
2205.3508534	0.23356240448E-02
522.35300699	0.19031022634E-01
167.73055542	0.89955758675E-01
62.670045373	0.26113248631

25.109749456 0.42348448173
10.225142681 0.24618926885
0 2 3 6.0 1.0
40.713442521 -0.30029667592E-01
5.6247090696 0.55575254864
2.2279949116 0.95581013442
0 2 1 0.0 1.0
0.83354741691 1.0
0 3 4 10.0 1.0
88.554315311 0.12728170015E-01
25.721525557 0.79394499843E-01
9.1278367624 0.24491506805
3.4312364064 0.40390526479
0 3 1 0.0 1.0
1.2308920645 1.0
0 3 1 0.0 1.0
0.39031845112 1.0
0 2 1 0.0 1.00
0.3249100 1.0
0 2 1 0.0 1.00
0.0812275 1.0

• Cd

48 22
0 0 8 2.0 1.0
1834021.925799246 0.0002627
652410.438011762 0.0005409
196643.061551306 0.0031220
63597.001731472 0.0108340
24337.097220192 0.0308145
9430.018012690 0.1047587
3764.731995088 0.2614361
1567.578467961 0.6709190
0 0 2 2.0 1.0
669.389311313 0.4705744
289.981985771 0.5605305
0 0 2 2.0 1.0
123.421652251 0.0065755
55.415790285 0.9941469
0 0 2 2.0 1.0
10.538249763 0.3907911
5.316831595 0.6292946
0 0 2 1.0 1.0
0.841316152 0.7269330
0.321816396 0.3067736
0 0 1 0.0 1.0
25.639845178 1.0
0 0 1 0.0 1.0
1.656184464 1.0
0 0 1 0.0 1.0
0.143785579 1.0
0 0 1 0.0 1.0

0.048680186	1.0
0 2 8 6.0 1.0	
16100.538573397	0.0004868
4077.294162925	0.0034697
1614.882168476	0.0110115
812.080304934	0.0304463
387.278771570	0.1011581
177.300362873	0.2586280
82.150981343	0.4195541
38.994293817	0.3317036
0 2 2 6.0 1.0	
17.910833888	-0.4218396
8.509952142	-0.6179470
0 2 2 6.0 1.0	
2.004202511	-0.5851014
0.999290497	-0.4506231
0 2 1 0.0 1.0	
4.034099663	1.0
0 2 1 0.0 1.0	
0.445731316	1.0
0 2 1 0.0 1.0	
0.044865658	1.0
0 2 1 0.0 1.0	
0.135521729	1.0
0 3 6 10.0 1.0	
544.076274629	0.0043976
166.732896419	0.0342675
63.984534896	0.1404980
27.186326930	0.3375677
11.970318298	0.4491481
5.372281062	0.2548613
0 3 1 10.0 1.0	
2.204454399	1.0
0 3 1 0.0 1.0	
0.849288912	1.0
0 3 1 0.0 1.0	
0.290103685	1.0
0 4 1 0.0 1.0	
2.2673870	1.0
0 4 1 0.0 1.0	
0.6891800	1.0

References

- ¹ E. Morra, G. Berlier, E. Borfecchia, S. Bordiga, P. Beato, M. Chiesa, *J. Phys. Chem. C*, **2017**, *121*, 14238-14245.
- ² E. Morra, M. Chiesa, *J. Phys. Chem. C*, **2018**, *122*, 9515-9522.
- ³ P. Höfer, A. Grupp, H. Nebenführ, M. Mehring, *Chem. Phys. Lett.* **1986**, *132*, 279-282.
- ⁴ S. Stoll, A. Schweiger, *J. Magn. Reson.* **2006**, *178*, 42-55.
- ⁵ G. Artioli, C. Lamberti, G.L. Marra, *Acta Crystallogr. B*, **2000**, *56*, 2-10.
- ⁶ M. Signorile, A. Damin, F. Bonino, V. Crocellì, et al., *J. Phys. Chem. C*, **2018**, *122*, 1612-1621.
- ⁷ C. W. Kim, N. H. Heo, K. Seff, *J. Phys. Chem. C*, **2011**, *115*, 24823-24838.
- ⁸ A. D. Becke, *J. Chem. Phys.* **1993**, *98*, 1372-1377.
- ⁹ Lee, C.; Yang, W.; Parr, R.G., *Phys. Rev. B* 1988, *37*, 785-789.
- ¹⁰ a) Fischer, M. *Phys. Chem. Chem. Phys.* 2016, *18*, 15738-15750; b) Fischer, M., *Phys. Chem. Chem. Phys.* 2015, *17*, 25260-25271; c) Signorile, M.; Damin, A.; Bonino, F.; Crocellà, V.; et al., *J. Comput. Chem.* 2016, *37*, 2659-2666.
- ¹¹ Grimme, S. *J. Comput. Chem.* 2006, *27*, 1787-1799.
- ¹² a) Mario Chiesa, Elio Giamello, Cristiana Di Valentin, Gianfranco Pacchioni, Zbigniew Sojka, and Sabine Van Doorslaer, *J. Am. Chem. Soc.* 2005 *127* (48), 16935-16944; b) Sara Maurelli, Gloria Berlier, Mario Chiesa, Federico Musso, Furio Corà, *J. Phys. Chem. C* 2014 *118* (34), 19879-19888.
- ¹³ Schäfer, A.; Huber, C.; Ahlrichs, R. *J. Chem. Phys.* 1994, *100*, 5829-5835.
- ¹⁴ Campos, C.T.; Jorge, F.E., *Mol. Phys.* 2013, *111*, 165-171.
- ¹⁵ Nada, R.; Nicholas, J.B.; McCarthy, M.I.; Hess, A.C., *Int. J. Quantum Chem.* 1996, *60*, 809-820.
- ¹⁶ Dovesi, R.; Saunders, V.R.; Roetti, C.; Orlando, R.; et al., *CRYSTAL17 User's Manual*. 2017.
- ¹⁷ Neese, F. Software update: the ORCA program system, version 4.0. *WIREs Comput. Mol. Sci.*, 2018, *8*, e1327.
- ¹⁸ a) Corma, A.; Mengual, J.; Miguel, P. *J. Appl. Catal. a-General* 2012, *421*, 121-134.; b) Ibanez, M.; Gamero, M.; Ruiz-Martinez, J.; Weckhuysen, B. M.; Aguayo, A. T.; Bilbao, J.; Castano, P. *Catal. Sci. Technol.* 2016, *6* (1), 296-306.; c) Signorile, M.; Bonino, F.; Damin, A.; Bordiga, S. *J. Phys. Chem. C* 2016, *120*, 18088-18092.
- ¹⁹ a) J. Datka, A. M. Turek, J. M. Jehng, I. E. Wachs, , *J. Catal.* 135 (1992) 186-199.; b) C.A. Emeis, *J. Catal.* 141 (1993) 347-354; c) Barzetti, T., Selli, E., Moscotti, D., Forni, L. *J. Chem. Soc. - Farad. Trans.* 92 (1996) 1401-1407
- ²⁰ J.W. Harris, M.J. Cordon, J.R. Di Iorio, J.C. Vega-Vila, F.H. Ribeiro, R. Gounder, *J. Catal.* 335 (2016) 141-154.
- ²¹ J. A. Weil, J. R. Bolton, J. E. Wertz, *Electron Paramagnetic Resonance – Elementary Theory and Practical Applications*, Wiley, New York, 1994
- ²² Fitzpatrick, J. A. J.; Manby, F. R.; Western, C. M. *J. Chem. Phys.* **2005**, *122*.
- ²³ R. F. W. Bader, *Atoms in Molecules. A Quantum Theory*; Oxford University Press: Oxford, UK, **1990**.